 doi:10.20944/preprints201811.0576.v1

Article

Optical micro-angiography (OMAG) based range optimization method for liquid flow rate

Peng Chen[1], Lei Jiang[1], Haixia Wang[1], Xiaorui Guo[2], Yilong Zhang[1], Yonghong He[2,3], and Ronghua Liang[1,*]

[1] College of Information and Engineering, Zhejiang University of Technology, Hangzhou 310023, China; chenpeng@zjut.edu.cn(P.C.); jianglei@zjut.edu.cn(L.J.); hxwang@zjut.edu.cn(H.W.); zhangyilong@zjut.edu.cn (Y.Z.)

[2] Shenzhen Key Laboratory for Minimal Invasive Medical Technologies, Institute of Optical Imaging and Sensing, Graduate School at Shenzhen, Tsinghua University, Shenzhen 518055, China; gxr15@mails.tsinghua.edu.cn (X.G.);heyh@sz.tsinghua.edu.cn(Y.H.)

[3] Department of Physics, Tsinghua University, Beijing 100084, China

* Correspondence: rhliang@zjut.edu.cn; Tel.: +86-139-5710-1740

Abstract: Optical micro-angiography (OMAG) is a new method of detecting flow rate and widely used for in vivo imaging. Although OMAG can distinguish between flowing and stationary parts, it cannot obtain accurate flow rate information. This study proposed a range formula for OMAG and the ultrahigh-sensitivity OMAG (UHS-OMAG) method to quantify the measurement range of an entire system. The parameters of the angle between beam scanning and flow directions, the angular velocity of the galvanometer, and the offset of incident light were introduced, and a formula for calculating the range was derived. Experiments were conducted to measure fine and ultra-fine flow rates by using OMAG and UHS-OMAG methods. The minimum measured flow rate was approximately 30 um/s, and the maximum measured flow rate was approximately 8 mm/s. Experimental results are in good agreement with the preset results.

Keywords: OMAG method; flow rate measurement; micro flow rate

1. Introduction

Optical coherence tomography (OCT) is a rapidly emerging optical imaging technology and a non-invasive imaging method [1,2] that is widely used in biology [3], medicine [4–6], and material research [7,8]. Doppler OCT (DOCT) was developed by combining the Doppler principle with OCT. Leigteb et al. implemented the first Fourier-domain OCT flow velocity detection experiment [9]. DOCT can determine the position and velocity of moving particles in high scattering media [10–12]. It can also be applied to microvascular in vivo imaging in medical diagnostics [13] and flow characteristic measurement in microfluidic monitoring [14], which has a good application prospect. However, DOCT can only measure velocity components parallel to the incident beam [15]. Therefore, the incident beam angle and the flow velocity direction (Doppler angle) must be accurately determined when calculating fluid velocity. However, the Doppler angle is difficult to measure in many practical applications. Consequently, DOCT cannot be used successfully in practical applications, especially those that involve living biological tissues.

To overcome these limitations, Wang et al. proposed optical micro-angiography (OMAG) technology in 2007 [16] and made several improvements [17,18]. OMAG is OCT micro-angiography based on complex signals. It utilizes the mathematical properties of Hilbert transform and constructs complex analytical signals using the Hilbert transform of real-interference signals. The structure and flow velocity information of a sample are obtained by Fourier transform. OMAG does not rely on the phase information of OCT, is not sensitive to environmental noise and other factors, and has made

great progress in terms of the sensitivity and image quality of flow rate detection [19]. In addition to its capability to achieve micro-structural imaging, OMAG provides volumetric vasculature images of the scanned tissue bed down to the capillary-level imaging resolution [20]. OMAG has a high application value in living microvascular imaging and has been successfully applied in human skin [21], cochlea [22,23], and human retina [24,25]. The ultrahigh-sensitivity OMAG (UHS-OMAG) method [26] was proposed to measure low flow velocities. This method remarkably improves imaging sensitivity.

Although changes in sensitivity in actual flow detection can be determined using the OMAG method, the method cannot effectively obtain the exact range of the system. Accurate flow rate information can be obtained when small flow rates, such as capillary flow rates, are detected. This information is limited in practical applications, such as medicine. For example, when measuring capillary information in the human body, the flowing particles in the capillaries can be separated from stationary particles, but the flow velocity information in the blood vessels cannot be accurately determined.

In this study, we derived a range calculation formula of OMAG and UHS-OMAG for the first time to quantify the system measurement range. We introduced the angle between beam scanning and flow directions, the angular velocity of the galvanometer, and the offset of incident light and derived a formula for calculating the range. Moreover, the images obtained within the measurement range were analyzed to explore the imaging patterns within this range. Our work provides the following contributions.

(1) After obtaining a rough estimate of the flow rate to be measured, the system's parameter values can be set according to the formula so that the measured image is displayed in the best imaging area.

(2) When the flow rate to be measured is unknown, the approximate range of unknown flow velocity can be calculated based on the measured image and parameter values of the system.

In our experiments, we estimated the flow rate by using our derived range formula, and the experimental results were consistent with the predicted results. We also analyzed the relationship between the intensity value of the obtained experimental result image and flow rate. A linear relationship was established between the intensity value of the image and flow velocity within the range.

2. System and theory analysis

2.1. System setup

The system used in this experiment is shown in Figure 1. The system consists of a superluminescent diode (SLD) as the light source with a center wavelength of 1310 nm and a bandwidth of 75 nm. The theoretical longitudinal resolution determined by the light source is 10 um. The light from the source is split into two paths through a 50:50 2×2 optocoupler. One light path is directed at a mirror called the reference arm, and the other light path is directed through the sample arm directly toward the sample. The light in the sample arm is coupled into an optical system that includes a collimator, a pair of X- and Y-axis galvanometers, and a 50 mm focal length objective with a theoretical lateral resolution of 17 um. The beam is reflected from the reference arm, and the sample arm is subsequently coupled into the detection arm and transmitted to a high-speed spectrometer to detect spectral interference signals. SENSORS' GL2048R linear array charge-coupled device (CCD) was the spectrometer used in this study. The number of pixels is 2048, the single pixel size is 10 um × 210 um, and the maximum sampling frequency is up to 147 kHz. The galvanometer imaging speed in our system is 600 mm/s, and the galvanometer reset speed is 3000 mm/s. The sampling frequency of the CCD and the scanning length can be changed in the program to modify the scanning frequency of the B scanning direction and the galvanometer speed of the Y galvanometer.

Preprints (www.preprints.org) | NOT PEER-REVIEWED | Posted: 26 November 2018 doi:10.20944/preprints201811.0576.v1

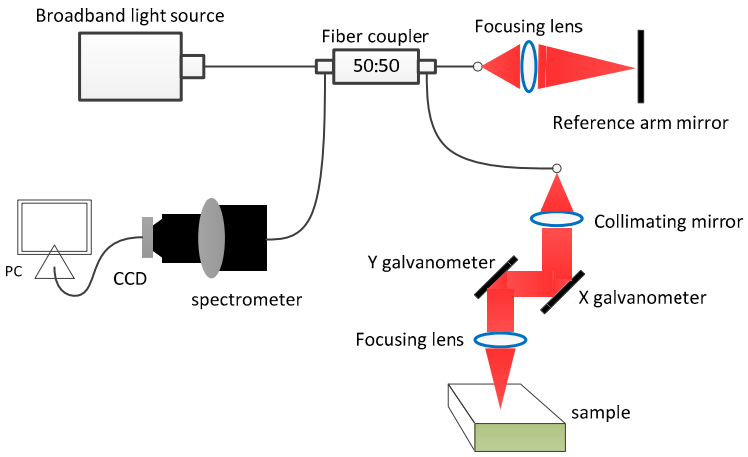

Figure 1. Schematic of the OMAG system used in this study.

2.2. Theory

The core concept of the OMAG method is to construct a complex analytical signal by using the Hilbert transform of the real-interference signal and obtain the structure and flow rate information of the sample by Fourier transform. Hilbert transform rotates the phase of a signal counterclockwise by 90°. We subsequently constructed an analytical signal whose imaginary part is the Hilbert transform of the real part. Then, we obtained structure and flow rate information in the signal by performing Fourier transform on the obtained analytical signal. Figure 2 shows that Hilbert and Fourier transform need to be performed in X and K directions, respectively, whereas traditional OCT can conduct Fourier transform directly in the K direction.

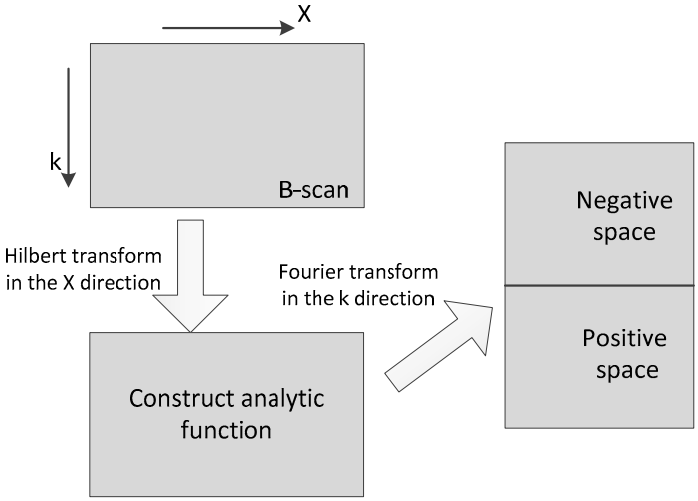

Figure 2. OMAG flow chart.

We can regard the 2D raw data obtained by OCT as a 2D array. The horizontal axis is time t, and the vertical axis is wave number k. We used a function with two variables to represent

$$B(k,t)=\cos\left[2kz_0+2\pi\left(f_C-f_D\right)t+\phi\right], \quad (1)$$

where z_0 is the initial depth position of the reflective particles at lateral position x and $\emptyset$ is a random phase term. f_C is the modulation frequency component, and f_D is the Doppler frequency component. Variables t and k are irrelevant, that is, when t changes, k is constant and vice versa. When the modulation frequency $f_C - f_D$ does not overlap with the signal bandwidth introduced by the random phase term, we can construct the analytic function of t by using the Hilbert transform constructor (1) based on the Bedrosian theorem [27]. In this case, the Hilbert transform of Equation

(1) is equal to its orthogonal representation, and $2kz_0$ is currently a constant phase term. If $f_C - f_D > 0$, then the analytic function of Equation (1) is

$$H(k,t) = \cos\left[2\pi(f_C - f_D)t + 2kz_0 + \phi\right] + j\sin\left[2\pi(f_C - f_D)t + 2kz_0 + \phi\right]. \quad (2)$$

If $f_C - f_D < 0$, then the analytic function of Equation (1) is

$$H(k,t) = \cos\left[2\pi(f_C - f_D)t + 2kz_0 + \phi\right] - j\sin\left[2\pi(f_C - f_D)t + 2kz_0 + \phi\right]. \quad (3)$$

Mathematically, Equation (3) is a complex conjugate form of Equation (2). We performed Fourier transform with k as the argument, where t is a constant term. The frequency component z_0 of Equation (2) is located in the positive space of the entire Fourier domain, and the frequency component of Equation (3) is located in the negative space of the Fourier domain. This part is the most critical in the OMAG approach.

The derivation shows that a fixed carrier frequency must be introduced to satisfy Hilbert transform and obtain a quadrature signal. The introduction of carrier frequency aims to add one item to the phase term of the interference signal, that is, a phase change occurs, and the phase change is the change in the optical path difference. Thus, the introduction of the fixed carrier frequency essentially causes the optical path difference to exhibit variety. This objective can be achieved by using two methods, namely, piezoelectric and offset. In the piezoelectric method, the piezoelectric ceramic drives the reference arm mirror to move at a uniform speed to introduce a carrier frequency. The offset method aims to make the collimating light of the sample arm deviate from the rotation center of the galvanometer to change the optical path and introduce a fixed carrier frequency.

The hardware of the piezoelectric OMAG method is different from that of a conventional frequency-domain OCT device. A piezoceramic needs to be installed on the reference arm mirror to drive the reference arm mirror to move at a constant speed and thus introduce a fixed frequency shift. We assumed that the reference mirror moves at a speed of v_{ref}, and the velocity of the moving particles in the direction of the probe beam is v_s. At this point, we can express the interferogram of the spectrum as

$$B(k,t) = \cos\left\{2k\left[z_0 + (v_{ref} - v_s)t\right] + \phi\right\}. \quad (4)$$

Equation (4) shows that when $v_{ref} - v_s > 0$, the region is imaged in the positive space. When $v_{ref} - v_s < 0$, the region is imaged in the negative space, and moving and static particles are separated.

The offset OMAG method introduces a fixed carrier frequency in such a way that the sample arm collimates light away from the center of the galvanometer. Compared with the piezoelectric method, the offset method does not require a single chip microcomputer or a driving circuit, and the entire system is simpler. Moreover, the piezoelectric method always moves while the reference arm mirror is moving during the scanning process. Thus, the spectrum of the returning light of the reference arm is constantly shaking, leading to additional noise in the resulting image. The offset method can also increase the imaging speed without adding a control module and without affecting the effect.

A schematic of the offset OMAG method is shown in Figure 3. In conventional frequency-domain OCT, the sample arm's collimated light is usually located at an angle of 45° relative to the initial galvanometer. We assumed that the optical path difference between the reference and sample arms is zero. The incident light subsequently moves downward by a distance of δ so that the incident light deviates from the rotation center of the galvanometer. After the incident light is reflected by galvanometer M, it is focused by objective lens L onto the focal plane. The focal length of the objective lens L is f, the distance between the rotation center of the galvanometer and the objective lens is d, and the rotation angle of galvanometer M relative to the initial position is α. The change in the optical path of the galvanometer during lateral scanning can be calculated by ray tracing as follows [28]:

$$OPD = \left[d\left(\frac{1}{\cos(2\alpha)} - 1\right) + \frac{\sin(\alpha)}{\sin(45^\circ - \alpha)}\sqrt{2}\alpha \right]. \quad (5)$$

Preprints (www.preprints.org) | NOT PEER-REVIEWED | Posted: 26 November 2018 doi:10.20944/preprints201811.0576.v1

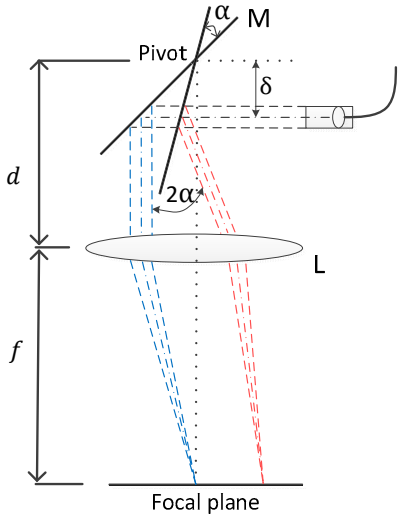

Figure 3. Schematic of the beam offset method at the sample arm.

3. Range derivation

Our derivation began with the piezoelectric OMAG method because the minimum measurement of piezoelectric OMAG is readily available. Then, a range calculation formula of the offset method was derived according to the relationship between the piezoelectric and offset OMAG methods. We also derived a range calculation formula of UHS-OMAG.

3.1. Derivation process

We generally have uneven high-scattering samples when detecting targets. Hence, the random phase term $\emptyset$ in Equation (1) varies randomly with time $(-\pi, \pi]$. The frequency component of $\emptyset$ with respect to t is a function of random distribution around zero frequency, and its bandwidth is BW. The envelope of this spectral distribution depends on the correlation between the interference signals at different positions of the sample. The bandwidth BW of this envelope is also limited by the sampling frequency f_s of the system. If BW and f_s are very close, then almost no correlation exists between the interference signals at different positions of the sample. We introduced modulation frequency f_c to obtain the analytical signal and subsequently remove its frequency band from the zero-frequency region until no overlap exists between the frequency band of the parsing signal and its complex conjugate frequency band. For its Hilbert transform to be strictly equal to its orthogonal form, the spectrum that corresponds to the phase term that changes over time is shifted to a position where no overlap with the zero frequency exists. We obtained the applicable conditions of the OMAG algorithm as follows:

$$f_c > \frac{BW}{2}. \tag{6}$$

BW determines the minimum speed that the system can detect. The smaller BW is, the smaller the value of f_c is and the lower the equivalent threshold speed is; hence, a small flow rate can be detected. In our derivation, the condition of BW < 2 f_c was always met.

The optical path difference (OPD) at this time in the piezoelectric OMAG method is the distance $v_{ref}t$ of the reference arm motion, the phase change is $2kv_{ref}t$, and the modulation frequency is $2k(v_{ref} - v_s)$, that is, the introduced carrier frequency f_C is kv_{ref}/π. Notably, v_{ref} and v_s in Equation (4) are vector representations. Relative to the movement of the reference mirror, the opposite movement of the particles reduces the difference in optical path length between the sample and reference arm and decreases the effective frequency of the modulation. When the value of v_s is sufficiently large, the moving particles are projected onto the positive space. In general, when the reference arm mirror moves toward the fiber coupler at speed v_{ref}, it is equivalent to the sample arm

Preprints (www.preprints.org) | NOT PEER-REVIEWED | Posted: 26 November 2018 doi:10.20944/preprints201811.0576.v1

that moves toward the galvanometer at velocity v_{ref}. At this time, only velocity v_s moves upward, and the particles of $v_s > v_{ref}$ are imaged on the dynamic plane. The same condition applies when the reference arm mirror moves in a direction opposite to the fiber coupler. Evidently, the minimum moving particle that can be measured by the piezoelectric OMAG method is greater than v_{ref}. In summary, we can obtain the lowest actual speed as follows:

$$v_{\min} = \frac{v_{ref}}{\cos\theta}. \tag{7}$$

In our work, the angle θ between beam scanning and flow directions was introduced for the first time to the range calculation of OMAG and UHS-OMAG. Notably, this θ is not the angle between the incident beam and the direction of flow velocity. Figure 4 shows that v_L is the scanning direction of the beam, v_F is the moving direction of the particles, and θ is the angle between v_L and v_F.

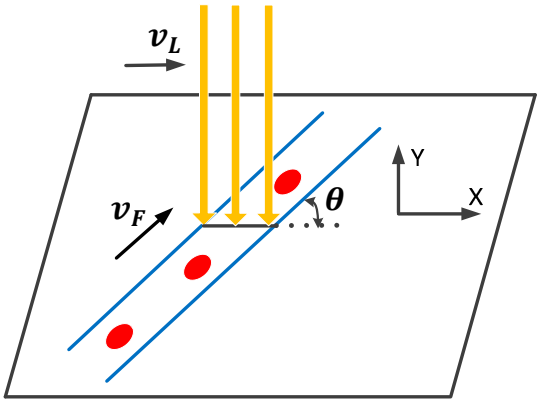

Figure 4. Schematic of the angle θ between the scanning direction of the beam and the direction of flow velocity.

In the conventional OMAG method, the phase difference between adjacent A lines in the B-scan is used to estimate flow velocity. Thus, the velocity during measurement is a component of v_F in X direction, and the measured velocity is $v_F \cos\theta$. In UHS-OMAG, the A-line density in B-scan is reduced, the scanning density of B-scan is increased, and the OMAG algorithm is applied to the C-scan direction. Therefore, the measured speed is v_F. A component of the Y direction, the measured velocity is $v_F \sin\theta$.

In the offset OMAG method, as indicated in Equation (5), α is small when our system collects data, and the first term in the equation is negligible compared with the second term when making phase changes. Thus, the phase change of the interference signal can be approximated as

$$\varphi = 4k\alpha\delta = 4k\delta\omega t. \tag{8}$$

where ω is the angular velocity of the X galvanometer and t is the scan time. Through the phase change, the change in the OPD of the offset method and the introduced carrier frequency value can be obtained, as shown in Table 1.

Table 1. Comparison of piezoelectric and offset methods.

	Piezoelectric method	**Offset method**
Optical path difference (OPD)	$v_{ref}t$	$2\delta\omega t$
Phase change (φ)	$2kv_{ref}t$	$4k\delta\omega t$
Introducing carrier frequency (f_c)	kv_{ref}/π	$2k\delta\omega/\pi$

A comparison of the two methods showed that the minimum speed that can be measured with the piezoelectric method is the velocity of the reference arm mirror v_{ref}, which can be obtained via conversion using the offset method as follows:

$$v_{\min} = \frac{v_{ref}}{\cos\theta} = \frac{2\delta\omega}{\cos\theta}. \tag{9}$$

 doi:10.20944/preprints201811.0576.v1

The maximum detection speed of the system is determined by the sampling frequency. According to the sampling theorem, the sampling frequency should be greater than twice the highest frequency component of the signal. Sampling frequency refers to time sampling, which is the sampling frequency f_{req} of the CCD. In summary, the range of an ordinary OMAG system is

$$v_{\max} = f_{req} \frac{\lambda}{4\cos\theta}. \tag{10}$$

3.2. UHS-OMAG range

Equation (9) shows that measuring a low flow velocity requires reducing BW and the galvanometer speed to obtain high sensitivity. However, BW cannot be reduced by reducing the diameter of the collimated light because the light source of our system is deterministic, and the effect of this method is limited. Thus, the speed of the galvanometer must be reduced to improve sensitivity. However, as the galvanometer speed decreases, the overall imaging process time increases considerably, thereby affecting the final image quality. Moreover, this method cannot achieve a remarkable increase in sensitivity, so the highly sensitive UHS-OMAG method was proposed. In contrast to the conventional OMAG method, UHS-OMAG reduces the density of A lines in the B-scan, increases the scanning density of the B-scan, and applies the ordinary OMAG algorithm to the C-scan direction. In the actual measurement process, ordinary OMAG only needs to complete a 2D scan, and the Hilbert transform structure analysis signal is implemented in the B-scan direction. UHS-OMAG must complete a 3D scan once and take an A line from each B-scan to form a 2D map. Subsequently, a Hilbert transform structure analysis signal is created for this 2D map. When using the offset method, the beam at this time needs to deviate from the rotation center of the Y galvanometer and not that of the X galvanometer.

Attention should be paid to the changes in range calculation when using the UHS-OMAG method. Compared with Equation (9), ω is no longer the angular velocity of the X galvanometer at this time. Instead, it is the angular velocity ω_Y of the Y galvanometer, δ is the distance δ_Y of the rotation center of the offset Y galvanometer, and f_{req} in Equation (10) is no longer the sampling frequency of the CCD but the scanning frequency f_B of B. The influence of angle θ between the beam scanning and flow velocity directions in the UHS-OMAG method should be given attention. In summary, the range of the UHS-OMAG method is

$$v_{\min} = \frac{2\delta_Y \omega_Y}{\sin\theta}, \tag{11}$$

$$v_{\max} = f_B \frac{\lambda}{4\sin\theta}. \tag{12}$$

4. Results and discussion

We used the offset method in the experiment. A capillary tube with an inner diameter of 0.4 mm was utilized as a channel, and milk was employed as a test fluid. A constant flow pump was used to provide a known steady flow rate.

From the system in Figure 1, we acquired spectral interference raw data from which the OMAG signal was calculated. We only needed a B-scan to process in the OMAG algorithm. In the 3D data block obtained by the acquisition system, we took Hilbert and Fourier transform from the acquired B-scan to complete the OMAG imaging. We obtained the spectral data matrix row by row to derive the analysis function using Hilbert transform. Then, we performed Fourier transform on the data matrix of Hilbert transform column by column. We divided the frequency components into positive and negative spaces of the Fourier domain. The flow partial region was imaged on a positive plane, and the stationary partial region was imaged on a negative plane. Positive plane imaging minus negative plane imaging resulted in an OMAG image.

4.1. OMAG range verification

Preprints (www.preprints.org) | NOT PEER-REVIEWED | Posted: 26 November 2018 doi:10.20944/preprints201811.0576.v1

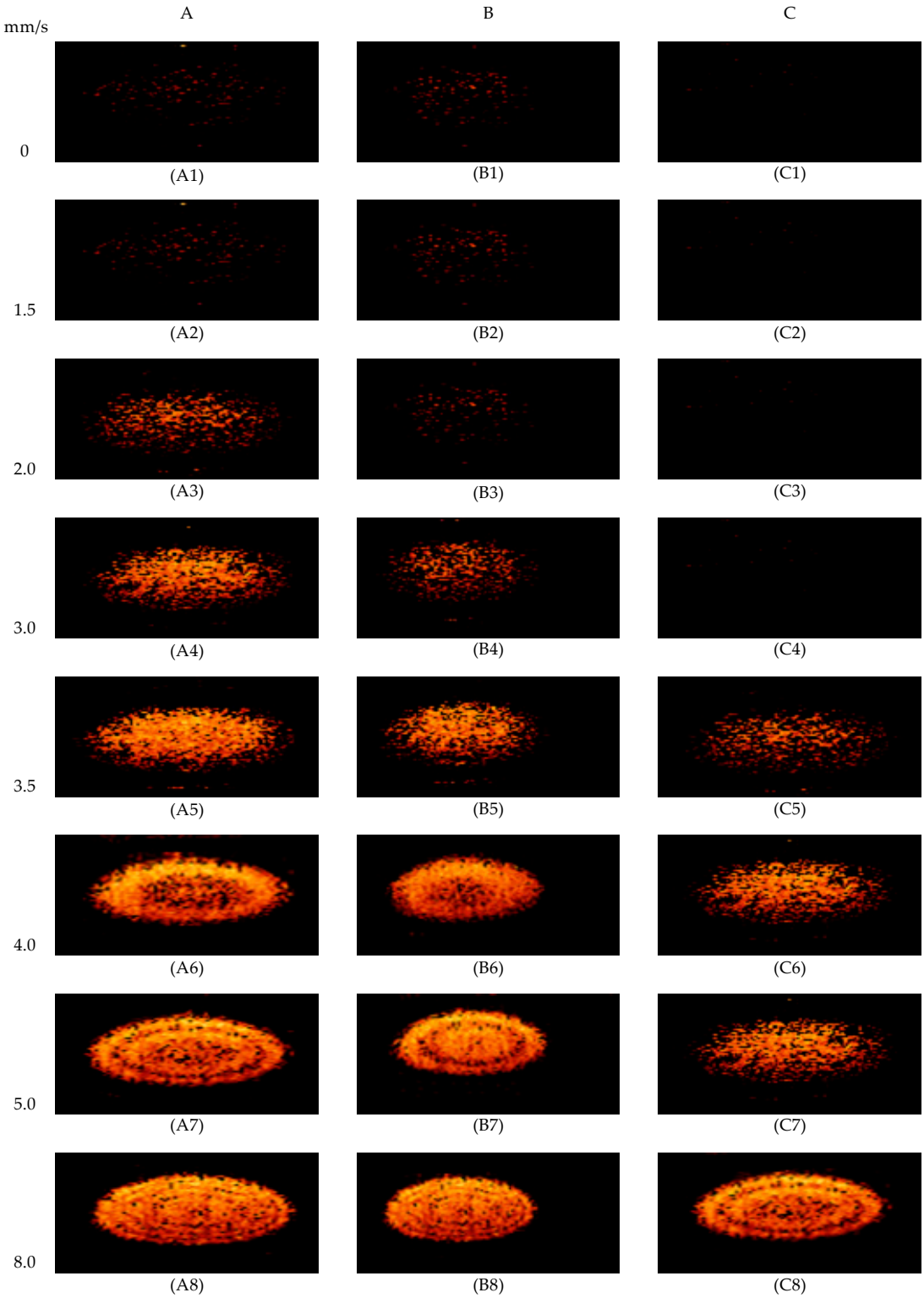

Figure 5. Experimental results of OMAG. The longitudinal direction is the same group of images at different flow rates, with the flow rate being gradually increased; the lateral direction is the experimental image of different groups at the same flow rat**e.**

We divided our OMAG experiment into groups A, B, and C. In the group A experiment, our B-scan direction length was set to 3 mm, the CCD sampling frequency f_{req} was 12 KHz, the scanning density was 500 lines/mm, the offset δ was 2.5 mm, and the galvanometer angular velocity was 24 mm/s. In the group B experiment, we did not change the other parameters, we reduced the scanning density to 200 lines/mm, and the galvanometer angular velocity was increased to 60 mm/s. In the group C experiment, the other parameters were unchanged compared with those in group A. The

 doi:10.20944/preprints201811.0576.v1

CCD sampling frequency f_{req} was increased to 24 KHz. We compared the variation in the range of angular velocity of the galvanometer based on the results of groups A and B. By comparing groups A and C, we determined the range when the CCD sampling frequency changed.

According to the parameters of our experimental system, the theoretical ranges of the three sets of experiments were calculated using Equations (9) and (10), as shown in Table 2.

Table 2. OMAG experimental parameter settings.

Group	f_{req}(KHz)	Scanning density (lines/mm)	δ (mm)	ω (mm/s)	Range (mm/s)
A	12	500	2.5	24	1.70–3.93
B	12	300	2.5	40	2.83–3.93
C	24	500	2.5	48	3.39–7.86

The pseudo color image results obtained through our experiments are shown in Figure 5, in which the leftmost side is the flow rate in mm/s.

The experimental results show that several images, such as A1 and A2 in group A; B1, B2, and B3 in group B; and C1, C2, C3, and C4 in group C, were not removed due to unavoidable slight jitter. Particles with an effective velocity were not screened out because their velocity was lower than the measurement range. In such a case, the imaging in each group was the same because the imaging images of A1 and A2 were the same.

As the speed increased, the particles that entered the range of the speed range were screened out. In the beginning, the velocity of the central portion of the test tube was higher than that of the wall portion, which conforms to the physical law. As the speed increased, many other particles entered the speed range, and the particles around the tube wall were also displayed. After the speed exceeded the range, some of the particles outside of this range were imaged onto the velocity plane, and some were imaged on the static plane. Phase winding occurred, and a circular pattern was created. In group A, the imaging at a flow rate of 2 mm/s was A3, at which point moving particles in the center of the test tube were already observed. As the flow rate and brightness increased, phase winding began to occur when the image was A6, and the measurable range was exceeded. In group B, when imaging B4 was just entering the range, imaging B6 was just beyond the range. In group C, when imaging C5 was just entering the range, imaging C8 was just beyond the range. The experimental results show that the detectable flow rates of groups A, B, and C were 1.7 to 3.9, 2.8 to 3.9, and 3.4 to 7.9 mm/s, respectively. This result is consistent with the range we calculated using the formula.

4.2. UHS-OMAG range verification

The UHS-OMAG experiment was performed differently in comparison with the ordinary OMAG method. UHS-OMAG requires a C-scan image in a 3D data block. We took all B-scan images, composed a 3D data block, and took a C-scan image from the block. To complete this process, we took out the A line of the same position of each B-scan in MATLAB and formed a C-scan image. Then, we processed the 2D spectrum of the reconstructed C-scan image and performed the same Hilbert and Fourier transform and subsequent processing as those in ordinary OMAG.

We divided our UHS-OMAG experiment into groups D, E, and F. In the group D experiment, the CCD sampling frequency was 60 kHz, the scanning density was 60 lines/mm, the B scanning direction length was 1 mm, the C scanning direction scanning density was 600 lines/mm, offset δ_Y was 2.5 mm, and the scanning length was 2 mm.

In the group E experiment, we only changed the length of the B-scan direction (set it to 2 mm). A change in the length of the B-scan direction would change the B-scan frequency and the speed of the Y galvanometer. In the group F experiment, we continued to increase the length of the B-scan direction and observed the change in the range.

The theoretical ranges for the three sets of experiments were calculated with Equations (11) and (12). In accordance with our system parameters, we obtained B-scan frequency (f_B) and Y-magnitude speed (ω_Y) (Table 3).

Preprints (www.preprints.org) | NOT PEER-REVIEWED | Posted: 26 November 2018 doi:10.20944/preprints201811.0576.v1

Table 3. UHS-OMAG experimental parameter settings.

Group	B-scan length(mm)	f_B(Hz)	δ_Y(mm)	ω_Y(mm/s)	Range (um/s)
D	1	750	2.5	1.250	85–347
E	2	375	2.5	0.625	44–174
F	3	250	2.5	0.417	29–116

The pseudo color image results obtained through our experiments are shown in Figure 6, in which the leftmost side is the flow rate in um/s.

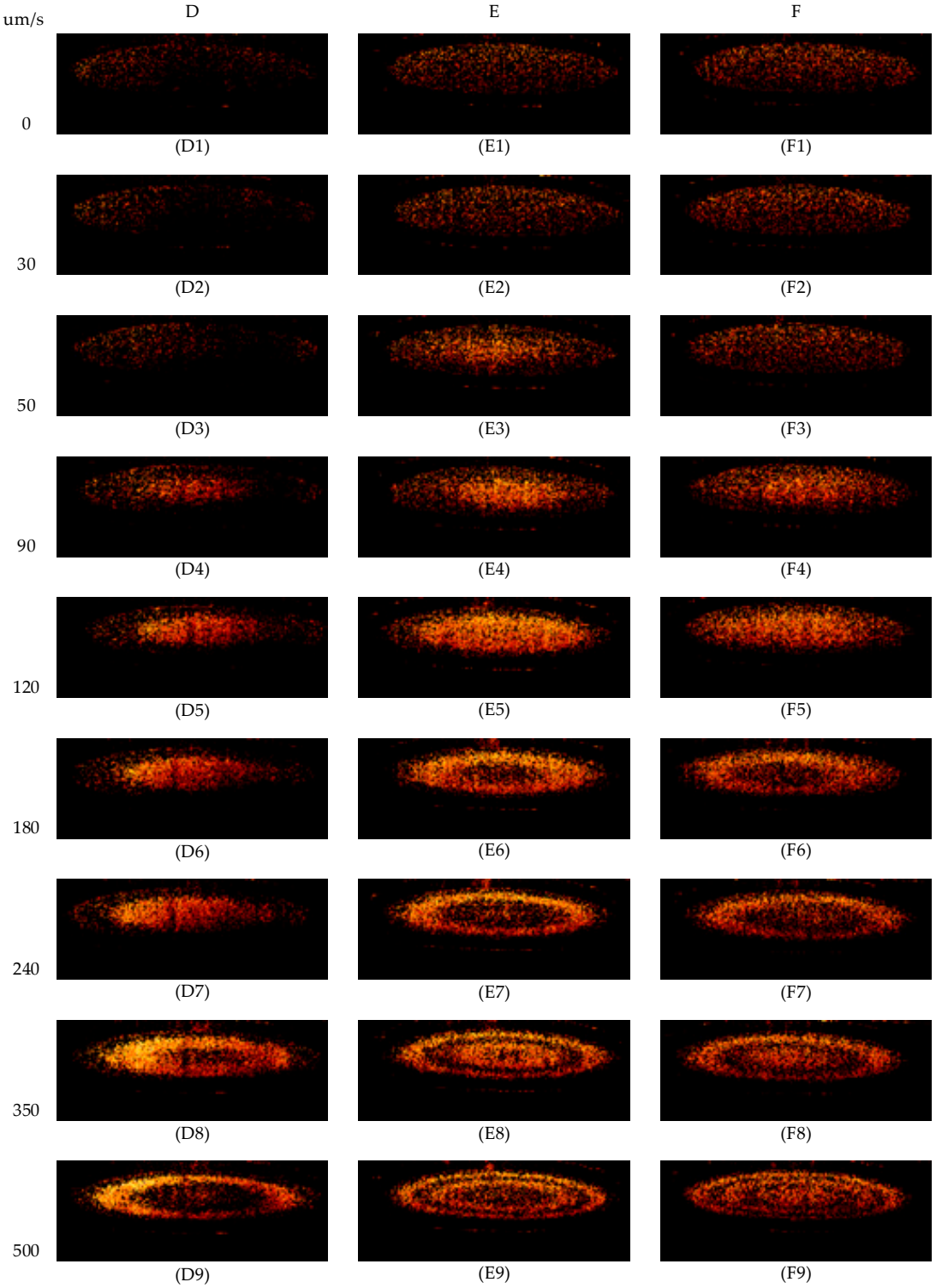

Figure 6. Experimental results of UHS-OMAG.

Preprints (www.preprints.org) | NOT PEER-REVIEWED | Posted: 26 November 2018 doi:10.20944/preprints201811.0576.v1

A comparison of images D1, F1, and E1 with A1, B1, and C1 showed that the mirror image that was not eliminated was more significant in the same state of 0 flow rate because the UHS-OAG method acquired more effects due to subtle jitter.

The same analysis was applied to group D. When imaging D4 was just entering the range, imaging D8 began to phase entangle beyond the range. In group E, when imaging E3 was just entering the range, imaging E6 began to phase entangle beyond the range. In group F, when imaging F4 was just entering the range, imaging F6 was just beyond the range. Our experimental results showed the flow rates detected by groups D, E, and F were 90 to 350, 50 to 180, and 30 to 120 um/s, respectively, which are consistent with the theoretical calculation range values in Table 3.

We processed all the collected data by using the UHS-OMAG method. The relationship between the average light intensity value and the flow rate of the obtained experimental image is shown in Figure 7.

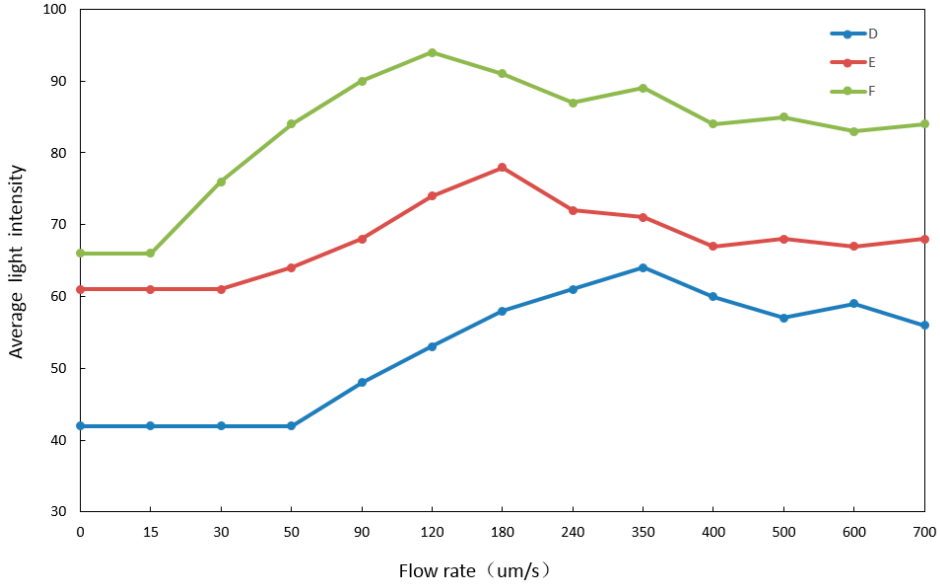

Figure 7. Relationship between average light intensity values and flow rate in the UHS-OMAG method.

When the flow rate was small, the jitter effect was not eliminated in all three cases; the higher sensitivity was, the greater the group influence was. In the range, the average light intensity value gradually increased as the flow rate increased. Beyond the range was exceeded, phase winding began to occur, and the average light intensity value began to fluctuate. Within the range, the intensity value of the imaged image was linear to the magnitude of the flow velocity.

5. Conclusions

We developed a flow rate range calculation formula for the common OMAG method and high-sensitivity UHS-OMAG method to quantify system sensitivity. We analyzed the piezoelectric OMAG method and the offset OMAG method. We used the variation in OPD and introduced the angle θ between beam scanning and flow velocity directions to accurately calculate the range under the OMAG method. The calculated range can be applied to normal OMAG flow rate detection and in the more sensitive UHS-OMAG method. We also obtained a linear relationship between the intensity value of the experimental image obtained under the OMAG method and the flow rate in the range by analyzing the experimental image. Our work is of considerable value in the practical application of the OMAG methodology in the future.

Author Contributions: conceptualization, P.C. H.W. and Y.H.; methodology, L.J., X.G. and Y.H.; software, X.G.; validation, L.J., X.G. and Y.Z.; formal analysis, L.J. and Y.Z.; investigation, P.C. and L.J.; resources, P.C.; data curation, X.G. and L.J.; writing—original draft preparation, L.J.; writing—review and editing, P.C, L.J. and H.W.; visualization, H.W.; supervision, R.L.; project administration, P.C.; funding acquisition, R.L.

Funding: This research was funded by the National Natural Science Foundation of China (NSFC), grant number 61527808.

Conflicts of Interest: The authors declare no conflict of interest.

References

1. Fercher, A.F.; Drexler, W.; Hitzenberger, C.K.; Lasser, T. Optical coherence tomography-principles and applications. *Rep. Prog. Phys*. **2003**, 66. 239-303.
2. Tomlins, P.H.; Wang, R.K. Theory, development and applications of optical coherence tomography. *Journal of Physics D Applied Physics*.**2005**, 38, 2519-2535.
3. Ravichandran, N.K.; Wijesinghe, R.E.; Lee, S.Y.; Choi, K.S.; Jeon, M.Non-Destructive Analysis of the Internal Anatomical Structures of Mosquito Specimens Using Optical Coherence Tomography. *Sensors*. **2017**, 17, 1897.
4. Tsai, M.T.; Tsai, T.Y.; Shen, S.C.; Ng, C.; Lee, Y.J. Evaluation of Laser-Assisted Trans-Nail Drug Delivery with Optical Coherence Tomography. *Sensors*. **2016**, 16, 2111.
5. Jansen, S.M.; Almasian, M.; Wilk, L.S. Feasibility of Optical Coherence Tomography (OCT) for Intra-Operative Detection of Blood Flow during Gastric Tube Reconstruction. *Sensors*. **2018**, 18.
6. Dimitrova, G.; Chihara, E.; Takahashi, H.; Amano, H.; Okazaki, K. AuthorResponse: Quantitative Retinal Optical Coherence Tomography Angiographyin Patients With Diabetes Without Diabetic Retinopathy. *Investigative Ophthalmology & Visual Science*. **2017**, 58, 190.
7. Shirazi, M.F.; Park, K.; Wijesinghe, R.E.; Jeong, H.; Han, S. Fast Industrial Inspection of Optical Thin Film Using Optical Coherence Tomography. *Sensors*. **2016**, 16.
8. Shirazi, M,F.; Jeon, M.; Kim, J. Structural Analysis of Polymer Composites Using Spectral Domain Optical Coherence Tomography. *Sensors*. **2017**, 17.
9. Leitgeb, L.; Schmetterer, W.; Drexler, A.; Fercher, R.; Zawadzki, T.; Bajraszewski. Real-time assessment of retinal blood flow with ultrafast acquisition by color Doppler Fourier domain optical coherence tomography. *Optics Express*. **2003**, 11, 3116-3121.
10. Wang, X.J.; Milner, T.E.; Nelson, J.S. Fluid flow velocity characterization by optical Doppler tomography. *Optics Letters*. **1995**, 20, 1337-1339.
11. Chen, Z.; Milner, T.E.; Dave, D.; Nelson, J.S. Optical Doppler tomographic imaging of fluid flow velocity in highly scattering media. *Optics Letters*. **1997**, 22, 64-66.
12. Izatt, J.A.; Kulkarni, M.D.; Yazdanfar, S.; Barton, J.K.; Welch, A.J. In vivo Doppler flow imaging of picoliter blood volumes using optical coherence tomography. *Optics Letters*. **1997**, 22, 1439-1441.
13. Bonesi, M.; Matcher, S.; Meglinski, I. Doppler optical coherence tomography in cardiovascular applications. *Laser Physics*. **2010**, 20, 1491-1499.
14. Veksler, B.; Kobzev, E.; Bonesi, M.; Meglinski, I. Application of optical coherence tomography for imaging of scaffold structure and micro-flows characterization. *Laser Physics Letters*. **2010**, 5, 236-239.
15. Ahn, Y.C.; Jung, W.; Chen, Z. Quantification of a three-dimensional velocity vector using spectral-domain Doppler optical coherence tomography. *Optics Letters*. **2007**, 32, 1587-1589.
16. Wang, R.K.; Jacques, S.L.; Ma, Z.; Hurst, S.; Hanson, S.R. Three dimensional optical angiography. *Optics Express*. **2007**, 15, 4083-4097.
17. Wang, R.K. Optical Micro angiography: A Label-Free 3-D Imaging Technology to Visualize and Quantify Blood Circulations Within Tissue Beds In Vivo. *IEEE Journal of Selected Topics in Quantum Electronics*. **2010**, 16, 545.
18. Wang, R.K.; An, L.; Saunders, S.; Wilson, D.J. Optical microangiography provides depth-resolved images of directional ocular blood perfusion in posterior eye segment. *Journal of Biomedical Optics*. **2010**, 15, 020502.
19. Wang, R.K.; Hurst, S. Mapping of cerebro-vascular blood perfusion in mice with skin and skull intact by optical micro-angiography at 1.3 mum wavelength. *Optics Express*. **2007**, 15, 11402-11412.
20. An, L.; Wang, R.K. In vivo volumetric imaging of vascular perfusion within human retina and choroids with optical micro-angiography. *Optics Express*. **2008**, 16, 11438-11452.
21. Baran, H.; Li, L.; Choi, W.J.; Kalkan, G.; Wang, R.K. High resolution imaging of acne lesion development and scarring in human facial skin using OCT-based microangiography. *Lasers in Surgery & Medicine*. **2015**, 47, 231-238.

22. Choudhury, N.; Chen, F.; Shi, X.; Nuttall, A.L.; Wang, R.K. Volumetric Imaging of Blood Flow within Cochlea in Gerbil in vivo. *IEEE journal of selected topics in quantum electronics: a publication of the IEEE Lasers and Electro-optics Society*. **2009**, 99, 1-6.
23. Subhash, H.M.; Davila, V.; Sun, H.; Nguyenhuynh, A.T.; Shi, X. Volumetric in vivo imaging of microvascular perfusion within the intact cochlea in mice using ultra-high sensitive optical microangiography. *IEEE Trans Med Imaging*. **2011**, 30, 224-230.
24. Liu, L.; Jia, Y.; Takusagawa, H.L.; Pechauer, A.D.; Edmunds, B. Optical Coherence Tomography Angiography of the Peripapillary Retina in Glaucoma. *Jama Ophthalmol*. **2015**, 133, 1045-1052.
25. Campbell, J.P.; Zhang, M.; Hwang, T.S.; Bailey, S.T.; Wilson, D.J. Detailed Vascular Anatomy of the Human Retina by Projection-Resolved Optical Coherence Tomography Angiography. *Scientific Reports*. **2017**, 7, 42201.
26. An, L.; Qin, L.; Wang, R.K. Ultrahigh sensitive optical micro angiography for in vivo imaging of microcirculations within human skin tissue beds. *Optics Express*. **2010**, 18, 8220-8228.
27. Bedrosian, E. A product theorem for Hilbert transforms. *Proceedings of the IEEE*, **2005**, 51, 868-869.
28. Wang, R.K. Use of a scanner to modulate spatial interferograms for in vivo full-range Fourier-domain optical coherence tomography. *Applied Physics Letters*, **2007,** 23, 3423-3425.